Supporting Information

Eichele *et al.*0708965105 10.1073/pnas.0708965105

SI Text

Group Independent Component Analysis. For clarity, we provide a detailed description of the group ICA model in the following section, complementing the graphical illustration in Fig. 2.

In this model, it is assumed that the fMRI signal is a linear mixture of statistically independent sources

$$s_p(v_p) = [s_1(v_p), s_2(v_p), \ldots, s_i(v_p)]^T,$$

indicated by $s_i(v)$ at location v for the ith source. The sources' weights at each location are multiplied by each sources' modulation over time. Hence, the N sources are linearly combined so that the data contains a weighted mixture of the sources. The linear combination of sources is represented by the mixing matrix A, and yields

$$u_p(v_p) = [u_1(v_p), u_2(v_p), \ldots, u_N(v_p)]^T,$$

representing N ideal samples of the signals $u_n(v)$. The sampling of brain activity with the MR scanner results in

$$y_p\,(i_p) = [y_1(i_p), y_2(i_p), \ldots, y_N(i_p)]^T,$$

where the fMRI is sampled at V voxels indicated by i = 1, 2,. . . ,T for the pth subject. A set of necessary transformations during preprocessing such as realignment, normalization and smoothing yields the effective spatial sampling for all subjects indexed by j = 1,2,. . . M, such that

$$y_p(j) = [y_1(j), y_2(j), \ldots, y_N(j)]^T.$$

The preprocessed data $y(j)$ were prewhitened and reduced to ${F_1}^{-1}. . . {F_M}^{-1}$ via temporal principal component analysis (PCA) retaining the major proportion of variance in the N uncorrelated timecourses of x

$$x(j) = [x_1(j), x_2(j), \ldots, x_N(j)]^T.$$

Then, group data were generated by concatenating individual principal components in the aggregate data set G^{-1}. Spatial ICA was performed on this set, estimating the optimal inverse of the mixing matrix (A^{-1}), and the aggregate components (C^{-1}), from which individual components were back-reconstructed.

Replicability Analysis. The fMRI data were first partitioned into eight spatially redundant sets by sampling the volume at every other voxel of the x, y, and z directions starting from the first or second slice, respectively, for computational feasibility, and to assess the replicability of ICs, measured by the spatial correlation across repetitions. Separately for each of the replications the data from each participant was prewhitened and reduced to 52 dimensions via PCA, retaining more than 95% of the nonzero eigenvalues. Individual PCs were then concatenated and reduced to a single aggregate set in which spatial ICA was performed, extracting a set of 52 independent components (ICs). Individual IC maps and timecourses were then back-reconstructed by multiplying the corresponding data with the respective portions of the estimated mixing matrix normalized to unit variance. The replicability of IC results was then assessed by measuring the spatial correlation between the results of the first analysis and the following runs, and aggregate ICs with spatial correlation exceeding $r > 0.8$ across all replications were further analyzed.

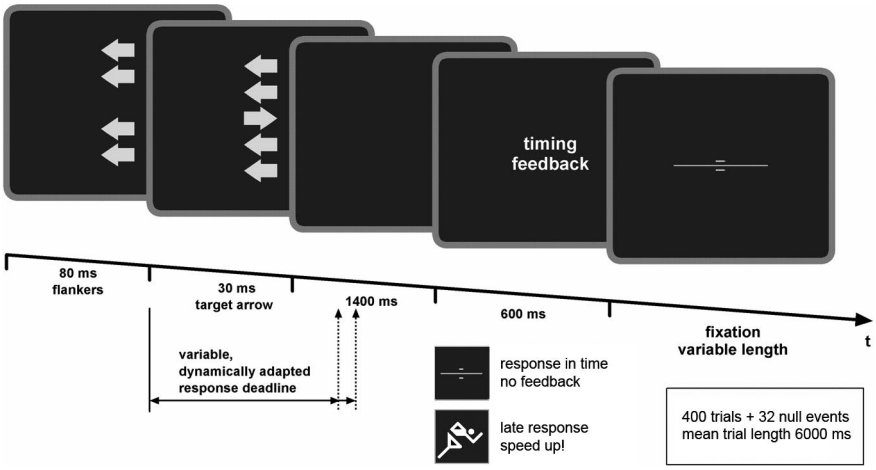

Fig. S1. Schematic representation of the Eriksen Flanker task. Stimuli appeared on a backprojection screen mounted inside the scanner bore behind the participants head. Throughout the experiment, participants were presented a central fixation mark. Participants performed a speeded forced-choice visual task, and had to respond with either a left or right hand button press following the direction of a central target arrow that was presented for 30ms and that was flanked by either response-compatible or response-incompatible arrows that were presented for 80 ms before the target. 50% of the flankers pointed into the same direction as the target (compatible trials), and 50% into the opposite direction (incompatible trials). Participants were instructed to respond as quickly and accurate as possible to the target with the response hand indicated by the arrow direction. For incompatible trials, response conflict arises because flankers and target arrow drive two competing response tendencies causing behavioral errors if the flanker-induced response tendency is executed. Whenever participants failed a dynamically adaptive response-time deadline, they were presented a symbolic feedback that appeared 600 ms after response onset, instructing them to speed up After a 1400ms blank screen a timing feedback (''speed up!'') was given if participants did not respond within a required time window. Participants received a pseudorandomized sequence of 400 trials at an average inter-trial interval of 6 seconds ($\pm$1.5 s jitter) and occasionally interspersed by null-events.

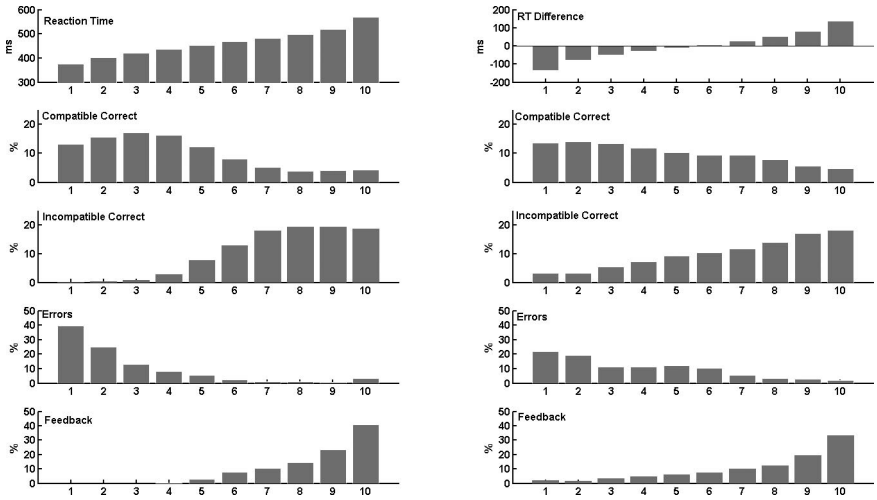

Fig. S2. Distribution of trials binned by response time (*Left*) and the differential of the response time (*Right*). To illustrate the relationship between conflict, accuracy and response time (RT), the trials of each participant were sorted into ten equally sized non-overlapping bins based on ascending RT speed (*x* axis), and the differential of RT (RT_0– RT_{-1}) to yield a histogram for each of the trial categories/outcomes. The group-averaged histograms are plotted for compatible, incompatible, error and feedback trials (*y* axis, in percent). Compatible trials and errors trials are usually fast, and incompatible trials and trials followed by a feedback are relatively slow. The interaction between RT and trial type therefore necessitated the removal of effects related to adjustment of response times in the hemodynamic data to ensure specificity of the inferences about error-induced and error-preceding activity.

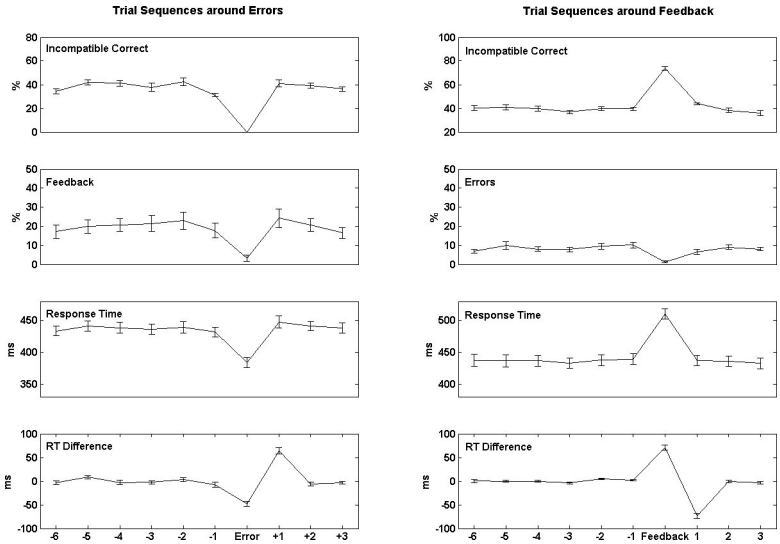

Fig. S3. Trial sequences around errors and feedback. To assess the possible confounding of behavioral errors and related brain activity with effects arising from conflict, feedback and response time, averages of trial type and timing in sequences from six trials before to three trials after error and feedback responses, respectively, were computed. Trials were grouped into sequences from six trials before to three trials after an error (*Left*) or feedback (*Right*), respectively, and averaged to check for bias in the distribution of trials surrounding the events of interest. This revealed the predicted effects, namely speeding at error and slowing at feedback trials, and subsequent adaptation processes expressed as posterror slowing and postfeedback speeding. However, the sequence preceding these events did neither over-represent compatible/incompatible trials, nor show relevant speeding/slowing over multiple trials. Trial categories are expressed as percentages, response times in milliseconds, error bars denote $\pm$ 1 standard error of the mean (SEM).

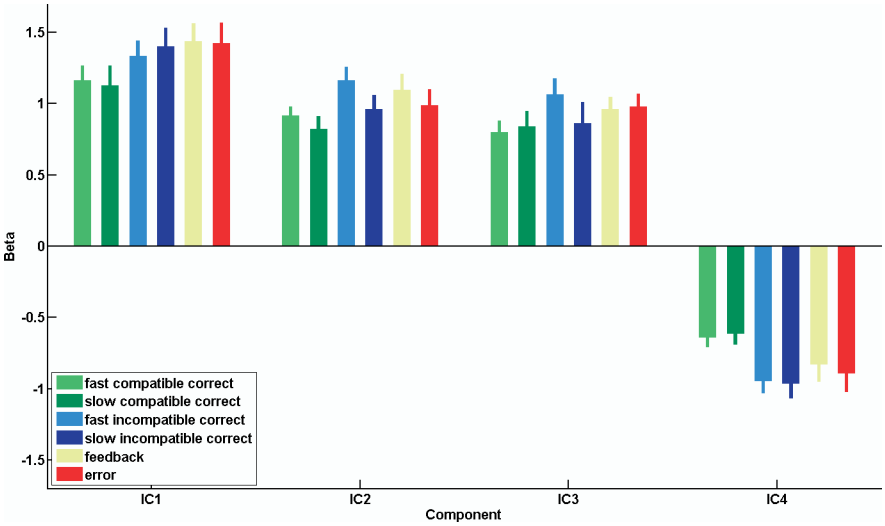

Fig. S4. Barplot of average component activations. Shown are the group-averaged beta weights (error bars denote standard error of the mean, S.E.M) from the single trial estimation for all components broken down into fast and slow trials via median split and separately for compatible, incompatible correct, feedback and error trials. All means were significantly different from zero magnitude (random effects), and the corresponding repeated measures ANOVA yielded significant differences between the means in all components.

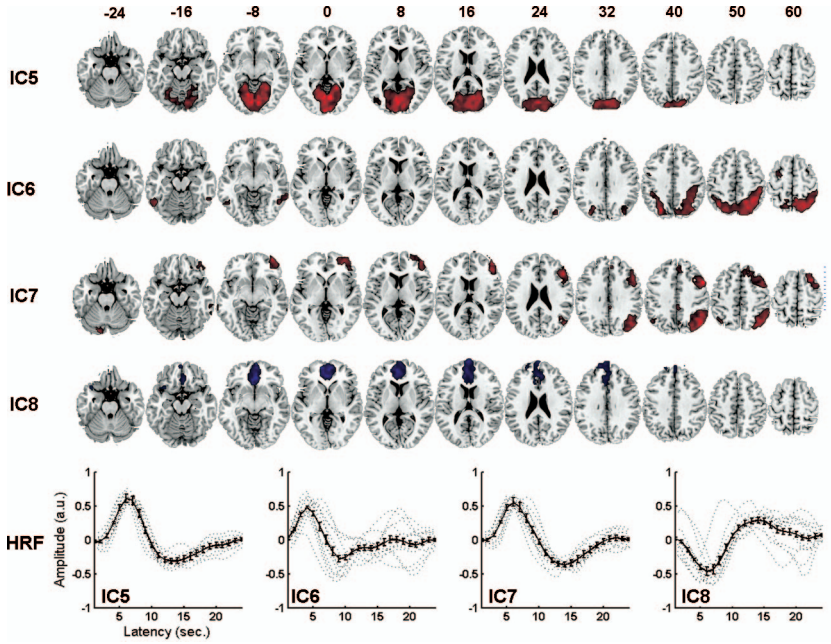

Fig. S5. Additional event-related components. IC 5, 6, 7, and 8 represent a set of generic components that were reliably identified across subjects and localized to the visual system, the dorsal and ventral attentional system anterior part of the DMN, respectively. These ICs showed robust event-related HRFs but were not modulated by the factors under investigation in the current task, and were thus not considered further. The IC maps are plotted at 1% false positive discovery rate threshold and at a cluster extent of at least 27 contiguous voxels. IC 5 was symmetrically localized in the lingual and calcarine gyri, and the cuneus, as well as a smaller cluster in the left middle occipital gyrus, thus representing visual cortex. IC 6 captured bilateral activity mainly in the superior occipital and parietal lobule, inferior temporal lobe, and the middle/superior frontal gyri, a pattern that appears largely consistent with the dorsal attention system. IC 7 on the other hand showed right-lateralized activation in the middle and superior frontal lobe, angular gyrus, and inferior parietal lobe, which is compatible with the ventral attention system. IC 8 is part of the default mode network (DMN) and showed a deactivation of regions in the frontal medial wall, including the anterior cingulate gyrus, medial superior frontal gyrus and gyrus rectus. Activations are plotted in red, deactivations in blue. The bottom of the figure displays the hemodynamic response functions for these four components from 1–20 seconds after stimulus onset, in arbitrary (range-scaled) amplitude units. The group average from the 13 participants is plotted as a solid line, error bars indicate $\pm$ 1 SEM, dotted lines represent individual HRFs.

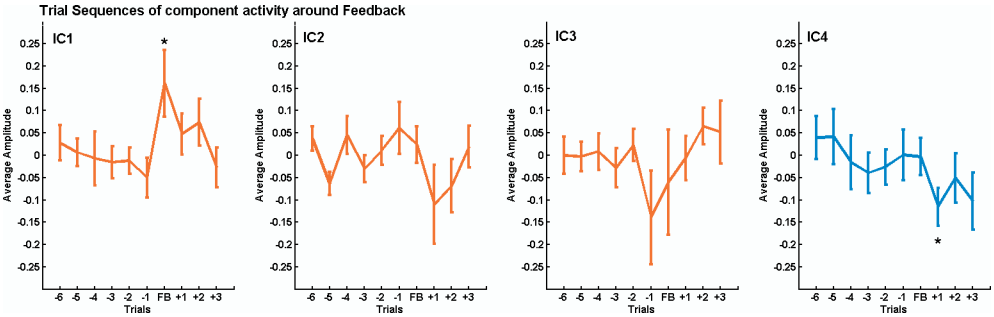

Fig. S6. Trial sequences of component activity around feedback. Group-averaged (±1 SEM) sequences of residual component activity from -6 to +3 around feedback (Trial 0) are shown for IC 1, 2, 3, and 4. A similar reengagement in the task was observed after a feedback was presented for trials with prolonged reaction times. In trials preceding feedback, IC 3 showed reduced activity on the average, but the t-statistics failed to reach significance. The monitoring system reflected in IC 1 showed a significant increase in activity on feedback trials. Subsequent to timing feedback, activity of IC 4 decreased significantly. A concomitant activity decrease of IC 2 was also found but also failed to reach significance.

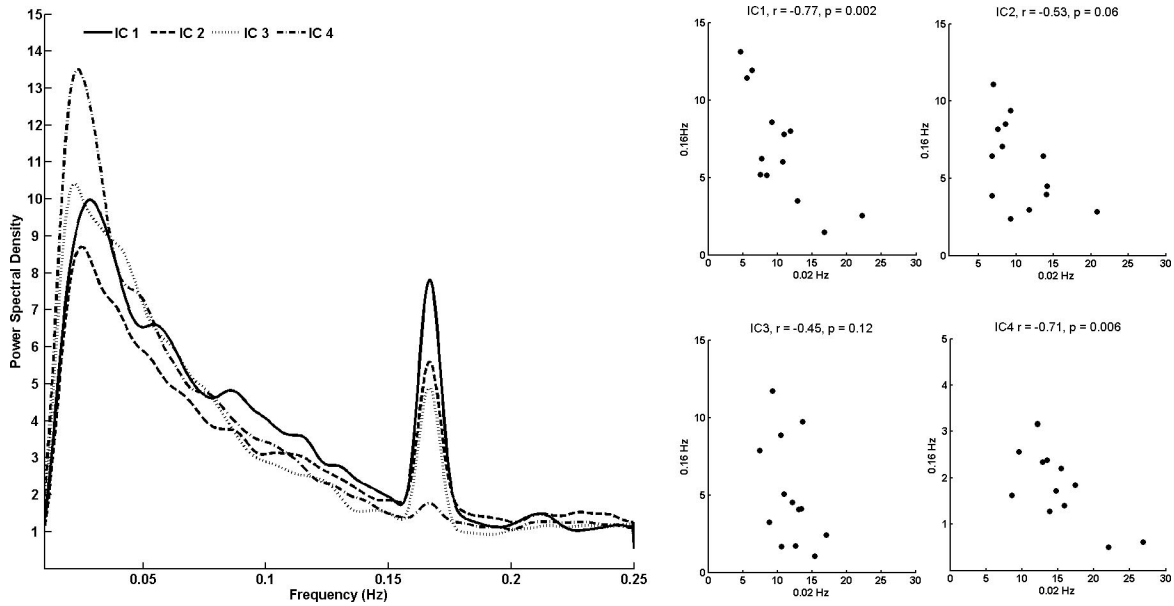

Fig. S7. Spectral analysis of component timecourses. One possible account for the slow trends preceding errors might be (phase-locked) low-frequency oscillations (LFO) in the fMRI signal at frequencies below 0.1 Hz. To explore this possibility, power spectral density (PSD) estimates were derived from the raw component time series. The spectra of the IC timecourses revealed a characteristic 1/*f* shape (cut off by the 72-sec high-pass filter) with peaks at about 0.02 Hz, and at 0.16Hz, the latter corresponding to a 6 seconds cycle as related to the trial-to-trial interval and the corresponding event-related HRF. In IC 1 and 4, the amplitude of these two peaks at 0.02 and 0.16Hz peaks were significantly anti-correlated, which was not the case in IC 2 and 3. Neither low frequency oscillations nor BOLD power spectral density peak amplitudes correlated with the number of errors or the number of feedbacks across subjects. To assess possible within-subject sequential effects, similar to those shown in the main manuscript, we performed a wavelet decomposition of the IC timecourses into scales with cycle lengths of 8, 16, 32, and 64 seconds. At the time-window around errors, oscillations in the low frequencies did not show a particular relationship to errors, neither did the higher frequency scales around 0.16 Hz fully account for the observed trends. We also repeated the deconvolution and single-trial estimation with different low-/high-pass filters on the IC timecourses and came to similar results, indicating that the trends preceding errors are a product of wide-band activity rather than specific frequencies. Also, neither the occurrence of errors nor the modulation of response times followed a 1/f distribution in these data. This means that although a correlation exists between higher and lower frequencies, we cannot tie any specific frequency to behavioral variability in this dataset.

Table S1. MNI coordinates of activation foci revealed by independent component analysis (putative main functions of components in current experiment are given in parentheses)

Region	Brodmann Area	*X*	*Y*	*Z*	*t*(max)
IC1 (performance monitoring)					
B RCZ	24/32	6	21	38	15,76
	24/32/8	6	29	34	12,52
	32/6	-2	14	42	12,91
B pre-SMA	6	2	14	49	10,67
	6	-6	10	53	12,65
	6	-2	14	45	12,22
B CCZ / SMA	24/31/6	6	-21	47	7,67
	24/31/6	-2	-13	47	5,84
R anterior superior insula	13	42	12	1	7,25
	13	42	8	5	6,08
L anterior superior insula	13	-38	16	5	8,26
	47	-42	19	-3	7,13
R inferior frontal gyrus, pars opercularis	44	53	13	20	6,75
L inferior frontal gyrus, pars opercularis	44/45	-53	15	-6	6,52
R posterior middle frontal gyrus/precentral sulcus	6	26	10	53	9,63
L precentral gyrus	6	-26	-5	50	9,26
	6	-42	-5	61	8,07
IC2 (sensorimotor)					
R precentral gyrus	4	38	-21	54	8,08
R central sulcus	3/1/2	42	-21	54	6,32
L postcentral gyrus	3	-38	-25	51	18,12
L central sulcus	4/3	-38	-24	58	13,83
L precentral gyrus	6	-18	-13	54	6,72
B SMA	6	2	-5	54	4,58
L superior frontal sulcus	6	-34	-4	68	6,53
L anterior orbital gyrus	11	-18	34	-17	6,06
L intraparietal sulcus, ascending branch	40	-38	-40	55	12,47
L supramarginal sulcus, parietal operculum	40	-53	-19	10	7,74
L inferior parietal lobule	39	-34	-48	59	5,34
IC3 (cost-benefit evaluation, effort)					
R inferior frontal gyrus / anterior inferior insula	47	30	23	-6	11,51
/ posterior orbital gyrus	13	30	23	-3	9,86
B posterior mesial frontal cortex	8m	2	30	48	9,64
	8m	2	33	41	7,07
	8m	-2	30	48	7,49
	8m	-2	33	41	6,18
IC4 (default mode)					
R precuneus/PCC/retrosplenial cortex	31	14	-57	27	12,20
	31	2	-57	27	11,59
	31	14	-53	19	10,47
	7	2	-64	31	8,39
L precuneus/PCC/retrosplenial cortex	31	-2	-57	27	11,72
	31	-2	-61	27	11,60
	7	-2	-64	31	8,21
	31	-10	-53	23	8,01
R Parahippocampal Gyrus	30	22	-50	8	5,69
L Lingual Gyrus	19	-14	-47	1	8,09
L Parahippocampal Gyrus	19	-18	-43	-3	7,39

RCZ, rostral cingulate zone; pre-SMA, presupplementary motor area; SMA, supplementary motor area; PCC, posterior cingulate cortex; R, right; L, left; B, bilateral.

Table S2. The functional connectivity between all four components was assessed by computing pairwise correlation coefficients between the single-trial estimates in each participant, and submitting the coefficients to one-sample *t* tests after Fisher *z* transformation

	IC1	IC2	IC3	IC4
IC1		t = 7.88, P <0.001	t = 2.88, P =0.01	t = -2.18, P =0.05
IC2	z = 0.29 ±0.04		t= 0.16, P= 0.88	t= -2.36, P=0.03
IC3	z=0.12 ±0.04	z=0.01 ±0.05		t=-4.69, P<0.001
IC4	z=-0.08 ±0.04	z=-0.10 ±0.04	z=-0.20 ±0.04	

Below the diagonal are the average z-transformed correlations, above the diagonal the corresponding t-statistic is given.

Table S3. Estimates of the predictive value of IC activity level for behavioural errors

Activity pattern $t_{-6..-1}$				Error rate (%) at t_0		Trial features at t_{-1}		
IC1	IC2	IC3	IC4	absolute	relative	Compatible (%)	Feedback (%)	RT (ms)
+	-	-	+	**12.88***	**47.93***	**46.44**	**18.31**	**−1.81**
+	-	+	+	11.16	28.11	47.01	19.12	**0.57**
+	+	-	+	10.15	16.50	48.99	14.78	**0.99**
+	+	-	-	9.34	7.23	50.00	17.17	**0.72**
-	+	+	-	9.30	6.83	50.17	17.28	**−3.12**
+	-	-	-	9.13	4.87	53.88	18.72	**−0.70**
-	-	-	-	8.55	-1.81	50.19	14.13	**−1.35**
+	+	+	-	8.53	-2.06	49.04	17.27	**0.02**
-	-	+	+	8.16	-6.26	46.60	14.63	**3.18**
-	-	-	+	8.16	-6.30	46.30	16.32	**-0.42**
-	-	+	-	7.97	-8.46	48.79	16.67	**−1.57**
-	+	+	+	7.84	-9.93	52.45	17.65	**0.35**
+	+	+	+	7.80	-10.41	49.65	20.92	**-0.83**
-	+	-	+	7.65	-12.20	50.77	15.29	**2.62**
+	-	+	-	6.75	-22.50	53.98*	15.03	**1.13**
-	+	-	-	**5.96**	**−31.52**	**54.59***	**22.48***	**0.59**

The change in error frequency relative to the absolute error rate (mean 8.69% ± 1.53, 95% CI 5.69–11.69) was computed for current trials (T_0) using a linear fit across the preceding five trials (T_{-6} to T_{-1}) of the residual activities of the four ICs in the sequence for all single-trial sequences pooled across all participants. Based on a mean split of the beta weights of the linear fit in the four ICs 16 nonoverlapping classes of trials were generated for which error rate at T_0, as well as the proportion of feedback (mean 17.06 ± 2.04, 95% C.I. 13.06–21.06), compatible trials (mean 49.56% ± 2.72, 95% C.I. 45.59 - 53.59), and average residual response time (mean -0.01ms ± 2.03, 95% C.I. -3.98 - 3.96) at T_{-1}.''+'' indicates larger than mean, ''-'' smaller than mean, ''*'' indicates $p<0.05$ (based on resampling).